Insights on the unique electro-catalytic behavior of PtBi/C materials

Bitty Roméo Serge Kouamé, Steve Baranton, Pascal Brault, Christine Canaff, William Chamorro-Coral, Amael Caillard, Karine de Oliveira Vigier, Christophe Coutanceau

Insights on the Unique Electro-Catalytic Behavior of PtBi/C Materials

B. S. R. Kouamé[1], S. Baranton[1], P. Brault[2], C. Canaff[1], W. Chamorro-Coral[2], A. Caillard[2], K. De Oliveira Vigier[1], C. Coutanceau[1],*

[1]IC2MP, UMR CNRS 7285, Université de Poitiers, 4 rue Michel Brunet TSA 51106, 86073 Poitiers, Cedex 9, France.

[2]GREMI, UMR 7344, CNRS - Université d'Orléans, BP 6744, 45067 Orléans Cedex 2, France.

Contact : christophe.coutanceau@univ-poitiers.fr

Abstract:

Molecular dynamics simulations have been performed to study the growth and the final structure of Pt_xBi_{1-x} clusters under conditions close to those encountered in classical low temperature chemical or physical synthesis methods, such as the water-in-oil route or plasma sputtering route, respectively. According to the simulations, Pt_xBi_{1-x} nanoparticles should consist in well crystallized Pt core surrounded by Bi structures, with strong interaction between Pt and Bi atoms. The simulation results were compared with physicochemical characterizations of Pt_xBi_{1-x}/C (x = 1.0, 0.9 and 0.8) materials synthesized at room temperature via the water-in-oil microemulsion method. XRD and XPS measurements led to the conclusion that Pt and Bi were not alloyed in Pt_xBi_{1-x} nanoparticles and that the nanoparticle surface was bismuth-rich, respectively, in perfect agreement with molecular dynamics simulations. XPS and electrochemical measurements allowed also demonstrating a strong electronic interaction between Pt and Bi, still in agreement with molecular dynamics. The electrocatalytic behaviors of the Pt_xBi_{1-x}/C catalysts have been studied. Pt_xBi_{1-x}/C displayed the higher activity towards glycerol electrooxidation in alkaline media, with an onset potential of ca. 0.300 V vs RHE and a unique selectivity towards glyceraldehyde/dihydroxyacetone formation for potentials lower

* ISE member

than 0.600 V vs RHE. A discussion on the relationship between composition/structure of the Pt_xBi_{1-x} catalytic materials and activity/selectivity for glycerol electrooxidation allowed proposing a mechanism involving a single-carbon adsorption mode on Pt and an electronic effect for the desorption of low oxidized species from Pt sites driven by the early stage of the Bi^0 to Bi^{II} transition.

Key-words: Activity, Bismuth, Electrooxidation, Glycerol, Molecular dynamics, Nanoparticles, Platinum, Selectivity

1. Introduction

With the depletion of fossil carbon, the use of renewable carbon which can come from vegetable oils or lignocellulosic biomass has received increasing interest. These feedstocks are rich of carbohydrates (cellulose and hemicellulose) in the case of lignocellulosic biomass[1,2], which are non-edible biopolymers coming from agriculture waste for instance, and of glycerol, which is a by-product of the production of biodiesel[3,4], in the case of vegetable oils. The conversion of these polyols and carbohydrates into value-added products has been extensively studied[5-8] owing to the large availability of these compounds. They are therefore now considered as green raw materials and platform molecules for the industries of the future.

Amongst all chemical reactions that can be performed from polyols and carbohydrates, selective oxidation reactions are very promising routes to synthesize building blocks for surfactants and polymers, as examples. Therefore, all oxidized species derived from bio-sourced polyols and carbohydrates are recognized to have important industrial interests[6,7]. However, strong oxidants, such as chromic acid, nitric acid or permanganate, have been used to perform oxidation reactions, but they are considered environmentally non-friendly and they led to non-selective formation of many undesired compounds[5,9]. It is still required to propose cleaner processes to selectively oxidize polyols/carbohydrates, that is the reason why catalytic and electrocatalytic methods have been developed. Recently, the development of electrocatalytic systems working either under direct fuel cell or electrolysis cell configurations[10-15] have received more and more attention.

In this context, platinum-bismuth (PtBi) and palladium-bismuth (PdBi) materials have been extensively studied for several decennia owing to their high catalytic activity towards controlled electrooxidation reactions of alcohols, polyols and carbohydrates[5,13, 16 , 17] . Intermetallic PtBi nanoparticles have also been shown to display high electrocatalytic activity towards formic acid electrooxidation. The synthesis of such well-ordered nanoparticles

necessitated either 9-12 h at reaction temperature of 735 °C [18] or three days at reaction temperatures between 145 and 160 °C[19]. However, PtBi catalytic materials must be produced with time and energy savings, i.e. at low temperature using rapid chemical or physical methods, such as spontaneous adsorption of Bi at the Pt nanoparticle surface, redox surface reaction, plasma co-deposition, etc. Colloidal methods are very interesting routes to obtain PtBi nanoparticles (NPs) under mild experimental conditions through wet chemistry synthesis. Amongst these colloidal methods, the water-in-oil microemulsion method has been shown to be very easy to implement and adapted for a wide family of metals.

The modification of Pt nanoparticles by bismuth has been shown to enhance the catalytic activity for glycerol oxidation and electrooxidation, and to orient the selectivity towards low oxidized species such as dihydroxyacetone and glyceraldehyde by both catalytic and electro-catalytic oxidation processes[5,13,16,20]. In the case of the electrocatalytic oxidation of glycerol, as an example, the onset potential was decreased by ca. 0.200 V on $Pt_{0.9}Bi_{0.1}$/C in comparison with that on Pt/C[13,20].

This unique catalytic behavior of PtBi catalysts must be understood with the scope of the optimization of electrooxidation reactions in terms of conversion yield, selectivity and efficiency. To achieve this, it is necessary to know the exact structure of the catalytic materials. This can be achieved by modeling the nucleation and growth process of PtBi nanoparticles to obtain information on the final structure and by comparing these results with experimental ones obtained from a comprehensive characterization of the catalytic materials. Such information could help to design the best material in terms of composition and structure. Herein, we will use molecular dynamics simulations to study the growth of Pt_xBi_{1-x} clusters under conditions close to those encountered in classical low temperature chemical or physical synthesis methods, such as the water-in-oil microemulsion or plasma sputtering routes, respectively. The simulation results will be compared with physicochemical characterizations of the Pt_xBi_{1-x} (x

= 1.0, 0.9 and 0.8) materials synthesized by wet chemistry. At last, a discussion on the relationship between composition/structure of the Pt_xBi_{1-x} catalytic materials and activity/selectivity of the glycerol electro-oxidation reaction will be proposed.

2. Experimental

Synthesis of carbon supported Pt, $Pt_{0.9}Bi_{0.1}$ and $Pt_{0.8}Bi_{0.2}$ nanomaterials.

Pt_xBi_{1-x}/C catalysts were prepared by mixing sodium borohydride (99%, Acros Organics) as reducing agent with a microemulsion carrying the metal salts ($H_2PtCl_6 \bullet 6\ H_2O$, 99.9% purity and anhydrous $BiCl_3$, 99.9 % purity from Alfa Aesar) dissolved in ultra-pure water (MilliQ® Millipore, 18.2 MΩ cm). Brij®L4 (Sigma Aldrich) was chosen as surfactant and the organic phase was n-heptane (99%, Acros Organics). Appropriate amounts of metal salts were dissolved to obtain a concentration of 0.10 mol L^{-1} (Pt^{4+} + Bi^{3+}). After the reaction process with $NaBH_4$, carbon powder (Vulcan XC72, Cabot Corporation) was added in the colloidal solution to obtain a nominal loading of 40 wt% metal on carbon and the mixture was kept under sonication for 1 h. The mixture was filtered on a 0.22 µm hydrophilic PVDF membrane filter (Durapore®, Millipore), rinsed with acetone and ultra-pure water. The carbon-supported catalyst was dried overnight in an oven at 75 °C.

Physicochemical characterization catalysts.

TGA. Thermogravimetric analyses were carried out with a TA Instrument SDT Q600 to determine the actual metal loadings of catalytic powders. Catalytic powder (ca. 3 mg) was put in an alumina crucible and heated under air from 25 °C to 900 °C with a temperature slope of 5 °C min^{-1}.

ICP-OES. Inductively Coupled Plasma – Optical Emission Spectroscopy measurements were performed using a Perkin-Elmer Optima 2000 DV.

AAS. Atomic absorption spectroscopy analyses were carried out with a Perkin Elmer AA200 Atomic absorption spectrometer.

TEM. Transmission electron microscopy measurements were performed using a JEOL JEM 2100 (UHR) with a resolution of 0.19 nm. The size distribution of the Pt-NPs as well as their mean particle size were determined using the Feret's diameter from the counting of 500 isolated NPs using the ImageJ free software.

XRD. XRD patterns were acquired using PANalytical Empyrean X-ray diffractometer. Measurements were performed from $2\theta = 20$ ° to $2\theta = 140$ ° in a step mode, with a step interval of 0.06 ° and a fixed acquisition time of 10 s at each value of 2θ. All XRD patterns were analyzed using the Levenberg − Marquardt method and deconvoluted using a pseudo-Voigt fitting by means of a computer refinement program (Fityk)[21].

XPS. XPS spectra were collected using a VG ESCALAB 3 MKII spectrometer using a monochromatized Mg K_α radiation (1253.6 eV). The source is operated at 300 W (15 kV and 20 mA). Powder analysis covered a surface of 2 mm × 3 mm. The binding energies are lined up with respect to the C 1s peak at 284.6 eV. The fits of the XPS spectra are carried out using a Shirley function for the background.

Electrochemical study of catalysts. Measurements were performed at 293 K in a conventional three-electrode electrochemical cell using a reversible hydrogen electrode (RHE) and a glassy carbon plate (3 cm^2 geometric surface area) as reference and counter electrodes, respectively. The working electrode was prepared by dispensing a catalytic ink onto a glassy carbon disc (0.071 cm^{-2} geometric surface area). The catalytic ink consisted in the dispersion of 17.7 mg of catalytic powder in 2.117 ml of ultra-pure water, 0.529 mL of 2-propanol (LC-MS CHROMASOLV®, Fulka) and 0.354 mL of Nafion® solution (5 wt% Nafion® perfluorinated resin solution in aliphatic alcohols). After homogenization in an ultrasonic bath (about 50 seconds), 3µL of catalytic ink was deposited on the freshly polished glassy carbon disc, leading to a metal loading of 100 μg_{metal} cm^{-2}.

First, nine cyclic voltammograms (CVs) were performed between 0.05 V and 1.00 V vs. RHE at the scan rate of 50 mV s^{-1} until stable CVs were obtained. Then, the 10th cyclic voltamograms were recorded between 0.05 V and 1.20 V vs. RHE in N_2-purged 0.1 M NaOH (Semiconductor Grade 99.99%, Aldrich) supporting electrolyte with a Model 362 Scanning Potentiostat from Princeton Applied Research at 5 mV s^{-1}.

Catalytic activity was studied by recording the stable third linear scan voltammograms at 5 mV s^{-1} in 0.1 M NaOH + 0.1 M glycerol (Reagent Plus ≥ 99%, Sigma Aldrich) solution in ultra-pure water using a PGZ 402 potentiostat from Voltalab.

3. Results and discussion

3.1 Molecular dynamics simulation of the growth of Pt_xBi_{1-x} clusters

Molecular dynamics (MDs) simulation is a very efficient method for the study of the growth and properties of nanoparticles,[22,23] because this method considers molecular scale processes. Basically, all the trajectories of a specie (atom, molecule) are calculated using the Newton second law, $\frac{d^2}{dt^2}\vec{r}(t) = -\overrightarrow{\nabla} V$, where $\vec{r}(t)$ represents the instantaneous position of each atom and V is the interaction potential between interacting atoms. The most important inputs for using such a calculation method are the expressions of interaction potentials and the set of initial conditions expected to match or to be representative of experimental conditions.

The PtBi nanoparticle synthesis by the water-in-oil microemulsion method is carried out at room temperature (25 °C). According the α-Pt-Bi phase diagrams described by Okamoto[24], at so low temperature and low bismuth atomic ratios, the solubility of Bi in Pt is negligible, and BiPt phases couldn't be formed. Therefore, it is important to get insights on the structure of materials because it will certainly drive electrocatalytic behavior of the catalysts. Because water-in-oil microemulsion occurs in a rather complex system (metal salts, water, oil phase, surfactant, reducing agent, hydrogen evolution during synthesis process, etc.), it is very difficult to model the particle growth from this synthesis route by MDs. Consequently, the

MDs simulations of PtBi material growth were carried out from plasma sputtering of platinum and bismuth atoms. For the initial conditions, the calculations are intended to describe the growth of Pt_nBi_{500-n} nanoparticles, where n represents the number of Pt atoms in the nanoparticle ($n \leq 500$) in the configuration of a gas aggregation source[25,26].

Briefly, a plasma is generated in a vacuum chamber by electrical breakdown between a negatively biased, magnetized electrode (magnetron target) and the surrounded grounded vessel in an argon low pressure atmosphere (10 Pa). Generated argon ions are bombarding the target made of the elements to be sputtered (Pt and Bi). The Ar pressure is high enough that the sputtered atoms can collide in the plasma creating nucleus which further continue to grow, while the energy of bond formation is released to the ambient gas. The simulation box ($L_x \times L_y \times L_z = 16 \times 16 \times 16$ nm^3) is thus composed of a mixture of Ar, Pt and Bi atoms randomly distributed, with typical ratios between Ar atoms and metal atoms in the vapor phase comprised between 2 and 10 [26]. In agreement with our experimental setup, a value of 8 corresponding to $n_{Ar} = 4000$ and $(n_{Pt} + n_{Bi}) = 500$, was chosen. The growth phenomena were studied for n_{Pt} = 400, 450 and 500 leading to clusters with atomic compositions of $Pt_{0.8}Bi_{0.2}$, $Pt_{0.9}Bi_{0.1}$ and Pt. The inputs imply that the collision number in the simulations will be less or equal to the actual one in real experiments and that the reactivity is not forced, if no event between two collisions or interactions is considered, which applies for the definition of the mean free path. To mimic the synthesis of PtBi nanomaterials by wet chemistry and to be as close as possible to the experimental conditions, the temperature of 300 K was used for the MDs simulations. The temperature of the Ar plasma was maintained around 300 K (with low fluctuations) by using a Berendsen thermostat. By transporting and dissipating the energy of clusters bond formation after collisions, the Ar atoms act as the solvent in the case of the synthesis of nanoparticles by wet chemistry. The Ar atoms act as a thermostat allowing the equilibration of the

temperature at 300 K before 10 ns, as it is proven by the crystalline core of the Pt nanoparticles formed.

The next step consisted in defining the interaction potentials. The Pt-Pt and Bi-Bi interaction potentials were treated by the very relevant Embedded Atom Method (EAM)[27-31]. The Pt-Bi interaction potential was built using the mixing rules suitable for EAM potentials[32]. The curves of interaction potentials as a function of the interatomic distance are shown in figure 1. Since the Pt-Bi bond strength is higher than those for Pt-Pt and Bi-Bi, it can be expected at a first sight that Bi atoms are located on the outermost surface. Moreover, the Pt-Bi equilibrium distance is larger than the Pt-Pt distance, which reinforces this expectation. The nanoparticle growth was monitored by integrating the equation of motions (time step of 1 fs) over a timescale of 10 ns (needing 10^7 iterations each), to fully complete the thermal relaxation of the whole system. Figure 2 display snapshots at 10 ns for all considered $Pt_{1-x}Bi_x$ atomic compositions.

The first important information is that the Bi atoms are always decorating Pt core clusters. The second one is that the Pt core is crystalline. Indeed, the atomic arrangement which can be observed in Figure 2 is typical of a crystalline structure of the Pt clusters, with numbers of 1st nearest neighbors between 10 and 12; (111) planes are also distinguishable. The third observation is that each cluster is stoichiometric, i.e. the Pt/Bi atomic composition is not only globally preserved but is also verified for each cluster. At last, the molecular dynamics simulation clearly indicates that for 20 at. % Bi ($Pt_{0.8}Bi_{0.2}$), the Pt core cluster is almost fully hidden by Bi atoms (Figure 2 c).

Inspection of the Bi organization on the Pt cluster cores shows that in the case of the $Pt_{0.9}B_{0.1}$ 50% of Bi atoms form dimers bonded to one Pt atoms (local bonding of $PtBi_2$). For the $Pt_{0.8}Bi_{0.2}$ atomic composition, 30% of Bi atoms form dimers (local bonding of $PtBi_2$) and 30% form trimers (local bonding of $PtBi_3$). It should be also noticed that the molar volume of Bi is 21

$cm^3\ mol^{-1}$ while that of Pt is 9 $cm^3\ mol^{-1}$. So, there is a strong hindering of the Pt surface atoms by Bi atoms. According to Solla-Gullón et al.[33], on Pt(111) one Bi atoms blocks three Pt sites. Therefore, it could be expected that the optimal composition for efficient catalytic conversion of molecules is Pt_xBi_{-x} with $x > 0.8$. In the case of $Pt_{0.9}Bi_{0.1}$ (Figure 2b), the Bi-free space makes Pt surface accessible, allowing enhancement of Pt activity through electronic interactions between Bi and Pt atoms and/or adsorption mode of molecules reacting at the surface.

3.2 Physicochemical characterization of Pt_xBi_{1-x}/C catalysts.

Pt/C, $Pt_{0.9}Bi_{0.1}$/C and $Pt_{0.8}Bi_{0.2}$/C nanocatalysts synthesized by a water-in-oil microemulsion method[11,13,20] at 25 °C were comprehensively characterized by different physicochemical characterization methods: TGA, ICP-OES, AAS, TEM, XRD, and XPS to access the loading, composition and structure of the nanocatalysts. Results are given in Table 1.

Thermogravimetric analysis allowed assessing the metal loadings on carbon, which were comprised between 37.5 wt% and 43.5 wt% (SI 1), i.e. close to the nominal loading of 40 wt% for all catalysts. The bulk composition of $Pt_{0.9}Bi_{0.1}$ and $Pt_{0.8}Bi_{0.2}$ NPs were determined by both ICP-OES and AAS. Both techniques led to very close compositions, which were consistent with the expected ones. TGA, ICP-OES and AAS characterizations evidenced the complete insertion in catalytic NPs of metals contained in microemulsions.

The mean sizes of the Pt/C and Pt_xBi_{1-x}/C NPs were determined from TEM photographs. Figure 3 display typical TEM images of isolated Pt/C (Figure 3a), $Pt_{0.9}Bi_{0.1}$/C (Figure 3c) and $Pt_{0.8}Bi_{0.2}$/C (Figure 3e), with the corresponding size distribution histograms in Figures 3b, 3d and 3f, respectively. The mean particle size for Pt/C was calculated to be ca. 5.2 nm, those for $Pt_{0.9}Bi_{0.1}$/C and $Pt_{0.8}Bi_{0.2}$/C to be both ca. 4.7. While the Pt nanoparticles are well dispersed on the carbon support, the PtBi nanoparticles tend to form agglomerates (not shown).

XRD patterns were recorded in the $20\ ° \leq 2\theta \leq 140\ °$ range (Figure 4). All the diffraction peaks were indexed to the face centered cubic (fcc) structure of Pt, and their position was found

to be consistent with the JCPDS 04 − 0802 card for platinum except for the small peak at 2θ = 23.1° in all patterns and a massive of peaks centered at ca. 30° in the case of $Pt_{0.8}Bi_{0.2}$/C, which were attributed to the {002} set of planes of turbostratic graphite[34,35] and to the presence of isolated small (amorphous) Bi oxide clusters[36], respectively. The mean crystallite sizes were determined from the full width at half maximum of the (111) diffraction peak at ca. 2θ = 40° related to the Pt fcc structure using the Scherrer equation and considering the approximation of spherical crystallites (shape factor K = 0.89)[37]. They were estimated in the range of 3.1 nm for Pt/C to 4.3 nm for $Pt_{0.9}Bi_{0.1}$/C. One must consider that due to strain/deformation effects inherent to nanoparticle with nanoscopic sizes, the crystallite sizes determined using the Scherrer equation is underestimated. It is worth to note the invariance of the position of the diffraction peaks related to the fcc structure with the increase of the bismuth atomic ratio in the Pt-based materials. The cell parameter values of the PtBi alloys (a_{Alloy}) calculated using the Bragg equation averaging the values of the four lattice parameters obtained for {111}, {200}, {220} and {311} planes are therefore very close to that of pure platinum (0.3916 nm), i.e. 0.3920 nm for $Pt_{0.9}B_{0.1}$ and 0.3926 nm for $Pt_{0.8}Bi_{0.2}$. According to Slater[38], the atomic radius of Bi is equal to 1.185 times the atomic radius of Pt (r_{Pt} = 1.185 r_{Bi}). The cell parameter of an alloyed fcc Pt_xM_{1-x} ($0 \leq x \leq 1$) bimetallic structure (a_{PtM}) can be calculated from the cell parameter values of pure Pt and M fcc structures, a_{Pt} and a_M, using the Vegard's law (Eq. 1):

$$a_{PtM} = x \times a_{Pt} + (1 - x) \times a_M \quad (1)$$

where a_{Pt} and a_{Bi} are expressed using equations (2) and (3) in the cases of Pt and Bi fcc structures, respectively:

$$a_{Pt} = 2 \times \sqrt{2} \times r_{pt} \quad (2)$$

$$a_{Bi} = 2 \times \sqrt{2} \times r_{Bi} = 1.185 \times 2 \times \sqrt{2} \times r_{pt} = 1.185\, a_{Pt} \quad (3)$$

leading in the case of Pt_xBi_{1-x} structures to,

$$a_{PtBi} = x \times a_{Pt} + (1-x) \times a_{Bi} = x \times a_{Pt} + 1.185 \times a_{Pt} \times (1-x) = a_{pt} \times (1.185 - 0.185x) \quad (4)$$

$a_{Pt_{0.9}Bi_{0.1}} = 0.3916 \times (1.185 - 0.9 \times 0.185) = 0.3988$ nm

$a_{Pt_{0.8}Bi_{0.2}} = 0.3916 \times (1.185 - 0.8 \times 0.185) = 0.4061$ nm

The changes in cell parameter values for $Pt_{0.9}Bi_{0.1}$ and $Pt_{0.8}Bi_{0.2}$ structures (0.3920 and 0.3926 nm, respectively) with respect to that for Pt (0.3916 nm) are not significant, and therefore it can be concluded that Pt and Bi are not alloyed (or very few) in the bimetallic materials.

At last, XPS measurements on fresh materials were carried out (Figures 5a,b,c,d) and revealed a total Bi atomic composition values for $Pt_{0.9}Bi_{0.1}$ (Figure 5b) and $Pt_{0.8}Bi_{0.2}$ (Figures 5d) catalysts 1.5 times to twice higher than the actual bulk ones as determined by AAS and ICP-OES, reaching 21 at% and 28 at% Bi, respectively. Because the mean escape depths of electrons by XPS are in the range of 1 to 2 nm for Pt and Bi[39] and the mean particle size of bimetallic catalysts is around 5 nm, the high Bi at% values indicated that bismuth was preferentially located close to the surface of the PtBi nanoparticles, accordingly to the MD simulations.

The Pt 4f profiles (Figures 5a,c) could be fitted by a single curve, according to the fit obtained on reference spectra recorded on Pt^0 (Casa XPS component parameters: LF(0.6,1.3,100,90)), centered at 71.2 eV which indicates that only Pt^0 oxidation state is present in both materials. In contrary, the Bi 4f profiles (Figures 5b,d) needed three or four mixed Lorentzian-Gaussian curves to be accurately fitted. From the positions of the peaks, the Bi $4f_{7/2}$ peak located at 157.5 eV, 158.3 eV and 159.7 eV could reasonably be assigned to the presence of Bi^0, Bi^{II} and Bi^{III} oxidation states[40], respectively. The peak at 161.4 eV is assigned to a tiny proportion of Bi^{IV}. Bismuth oxide structures concentrated mainly on the platinum surface were already observed by Kimatura et al.[41] for 1% Bi-5% Pt/C catalyst synthesized by reduction of chloroplatinic acid and bismuth chloride by sodium borohydride in alkaline solution.

Because the electrocatalytic measurement were performed on "activated" Pt_xBi_{1-x}/C catalysts, after 10 cycles in supporting electrolyte between 0.05 V and 1.00 V vs RHE to obtain stables CVs over the time scale and potential range of the experiments, XPS spectra were also recorded on the "activated" catalysts after stopping the last CV at ca. 0.05 V vs RHE (Figure 5 e,f,g,h). The ratios of the different species are given in Table 1. The atomic ratios of platinum remain constant. It is worth to note that the ratios of highly oxidized Bi^{III} and Bi^{IV} atoms is always, before and after cycling, much higher in $Pt_{0.8}Bi_{0.2}$ than in $Pt_{0.9}Bi_{0.1}$. This indicates that higher number of bismuth atoms in $Pt_{0.8}Bi_{0.2}$ are less or not interacting with platinum. It is also worth to note that no Bi^0 was detected after cycling. This result was surprising because, according to other authors, Bi should be metallic at a so low potential[42,43]. However, results are provided by *ex-situ* XPS measurements, and small clusters of Bi^0 (MDs simulations predicted the formation of Bi dimers and trimers at the Pt surface) could be oxidized in air into Bi^{II} during the transfer of the electrode from the cell to the XPS chamber.

To summarize the above characterization results, the actual metal loadings and bulk atomic ratios are close to the expected (nominal) ones, Pt and Bi atoms are not alloyed and the nanoparticle surface is bismuth-rich. Therefore, the PtBi materials prepared by the water-in-oil micro-emulsion route consist in Pt nanoparticles of ca. 5 nm diameter surrounded by bismuth structures, in agreement with the molecular dynamics calculation in section 3.1. According to XPS results, bismuth atoms are under different oxidized states, forming likely $Bi^{(}OH)_2$ as main structure, as well as $Bi(OH)_3$ and/or Bi_2O_3 structures, although the presence of Bi^0 after potential cycling and stop at 0.05 V vs RHE is also very likely. At last, the higher is the bismuth atomic ratio, the higher is the highly oxidized bismuth atom proportion in the samples, i.e. atom proportion less or not interacting with platinum.

3.3 Electrochemical characterizations of Pt_xBi_{1-x}/C catalysts.

Because electrocatalytic reactions take place only at the surface of the catalytic materials, gaining information on their surface structure is of paramount importance. Electrochemical methods are very powerful to study the surface structure of materials since only surface atoms which can be electroactive are probed and the surface structures are determined in the environment of their use. Figures 6a displays the tenth stable cyclic voltammograms (CVs) of Pt_xBi_{1-x}/C materials in 0.1 M NaOH N_2-saturated electrolyte recorded between 0.05 and 1.20 V vs RHE. The Pt/C catalyst gives the typical CV shape (black line) of polycrystalline platinum nanoparticles in a clean alkaline electrolyte. The first 9 CVs between 0.05 V and 1.0 V vs RHE of $Pt_{0.8}Bi_{0.2}/C$ showed no significant changes in shape and only a very small decrease in oxidation and reduction current, whereas no change was observed on $Pt_{0.9}Bi_{0.1}/C$ (SI 2). These observations speak towards the preservation of the structures of fresh catalysts upon the ten first voltammetric cycles.

The CV of $Pt_{0.9}Bi_{0.1}/C$ (red line) shows a (quasi) total inhibition of the hydrogen underpotential deposition (H_{UPD}) and H_{UPD} desorption, as the typical redox feature in the so-called hydrogen region between ca. 0.05 and 0.40 V vs RHE are not present, in agreement with previous observations[44]. This suggests either a (quasi) full coverage of Pt surface by Bi structures or an electronic effect of Bi on Pt inhibiting the hydrogen adsorption process. From 0.25 V vs RHE a low positive current slightly increases with potential and for potentials higher than 0.40 V vs RHE, two oxidation peaks are observed centered at 0.62 and 0.82 V vs RHE, the first one appearing before and the second one superimposing with the Pt surface oxidation process. Indeed, the oxidation current recorded after the peak centered at 0.82 V vs RHE, i.e. between ca. 0.90 V and 1.20 V vs RHE, originates from the Pt oxidation process[45]. The facts that the Pt surface is covered by bismuth species and that the Pt surface oxidation still happens at high potentials suggest that part of the Pt surface is accessible for oxidation reaction, which seems in contradiction with the inhibition of hydrogen adsorption/desorption process, but in

agreement with MDs simulations. However, MDs simulations indicated that in the case of $Pt_{0.8}Bi_{0.2}$ the Pt surface coverage by bismuth atoms was very high, but the Pt surface oxidation process appears completely not affected. From those observations, it results that either dissolution of bismuth upon oxidation, or reorganization of bismuth on Pt surface, or oxygen transfer between bismuth oxide species and platinum surface occurs allowing the oxidation of the latter. In the case of polycrystalline Pt electrode modified by Bi adatoms, Kardigan et al.[45] proposed that the main oxidation peak that they observed at ca. 0.85 V vs RHE was related to the redissolution of Bi, whereas the cathodic one at ca. 0.73 V vs RHE was related to Bi underpotential deposition. CVs recorded before and after 1000 potential cycles between 0.05 and 1.00 V for Pt/C, $Pt_{0.9}Bi_{0.1}$/C and $Pt_{0.8}Bi_{0.2}$/C are presented in Figure 6b. After 1000 cycles, the Pt/C catalyst undergoes dramatic loss of surface area whereas the capacitive current in the double layer region remains almost constant. Such phenomenon was already observed in alkaline media and was attributed either to Pt particle detachment from the carbon surface[46] or to corrosion/dissolution of Pt nanoparticles[47]. However, by comparing polarization curves recorded on Pt/C in figure 7a and 7b, one can remark that the loss in active surface area of Pt/C has little impact on the catalytic activity towards glycerol electrooxidation.

The CV after 1000 cycles for $Pt_{0.9}Bi_{0.1}$/C remains almost similar as the one after 10 cycles, indicating the very good stability of this catalyst. In this case, at least, the dissolution/redeposition mechanism appears not convenient because it would be reasonable to expect that a continuous loss of bismuth by dissolution occurs. The rearrangement of Bi atoms with the electrode potential, like a breathing process (Pt fully covered with Bi^0 species at low potentials and partially covered with Bi_2O_3 or $Bi(OH)_3$ species at high potentials) cannot be discarded. Another reasonable hypothesis concerns the possible reversible spill-over of oxygen between Bi and Pt at the nanoparticle surface.

In contrary, the CV after 1000 cycles for $Pt_{0.8}Bi_{0.2}/C$ is greatly modified compared with the one after 10 cycles. The changes in CV shape over the 1000 voltammetric cycles are presented in SI 3 every 100 cycles for a sake of clarity. The shape changes drastically from the first to the 500^{th} cycles and then stabilize for higher number of cycles. The redox features between 0.10 V and. 0.55 V vs RHE have completely disappeared and the CV resembles closely that of $Pt_{0.9}Bi_{0.1}/C$. In this second case, dissolution of bismuth species likely takes place until reaching a stable surface structure close to that of the stable $Pt_{0.9}Bi_{0.1}/C$ material. This suggests that different kinds of bismuth atoms exist, those that can be dissolved and those that cannot be dissolved. In this context, the redox feature from 0.10 V to 0.55 V vs RHE in the $Pt_{0.8}Bi_{0.2}/C$ CV profile is due to Bi atoms not interacting with Pt, and which dissolve upon potential cycles, whereas the remaining redox features in the range from 0.25 V to 0.90 V vs RHE are due to stabilized Bi atoms in interaction with Pt.

It is worth to note that the current plateau for potentials in the range from 1.00 to 1.20 V vs RHE for the positive scan direction is not affected by potential cycling in the case of $Pt_{0.9}Bi_{0.1}/C$ and $Pt_{0.8}Bi_{0.2}/C$ materials, whereas it displays lower current density values after 1000 potential cycles for Pt/C. This suggests that the presence of bismuth protects the Pt nanoparticles from degradation.

XRD patterns were recorded on $Pt_{0.9}Bi_{0.1}/C$ and $Pt_{0.8}Bi_{0.2}/C$ electrodes before (fresh) and after (aged) 1000 cycles between 0.05 V and 1.00 V vs RHE and compared with that of a Pt/C catalyst in order to check if PtBi alloys could be formed upon cycling (SI 4). No change in XRD peak positions is observed, which indicates that no alloy is formed and that the Pt core Bi shell structure of the fresh catalysts is conserved after 1000 cycles between 0.05 and 1.00 V vs. RHE.

Considering the negative potential scan, the sharp reduction peak centered at ca. 0.70 V vs RHE is followed by a shoulder at ca. 0.50 V vs RHE. The first intense reduction peak at high

potentials is related to both the reduction of bismuth oxides formed in the oxidation peak centered at 0.82 V vs RHE and to the reduction of platinum surface oxides, whereas the shoulder at lower potentials is related to the reduction of bismuth oxide species formed in the oxidation peak centered at ca. 0.62 V vs RHE. It is worth to note that the oxidation peak centered at 0.82 V and the feature related to Pt surface oxidation starts at the same potential, and that reduction of bismuth oxide species formed from 0.70 to 0.90 V and of platinum surface oxides leads to a unique reduction peak. Both these observations suggest strong interactions between both metals (bismuth species in contact with platinum, in total agreement with MDs calculations).

Zuo et al.[40] investigated the change of the Bi valence state in a Bi_2O_3 electrode along the cathodic linear sweep voltammetry in Na^+ containing aqueous electrolyte using *ex situ* XPS. By following the changes in the Bi 4f XPS peaks, they concluded that Bi_2O_3 can be firstly reduced into Bi^{II} and then to elemental Bi^0 during the cathodic process, which also explained the appearance of two anodic CV peaks (oxidation from Bi^0 to Bi^{III} bridging with Bi^{II}). The CV of $Pt_{0.8}Bi_{0.2}/C$ (blue line in Figure 6a) points out, in addition to the same features as for $Pt_{0.9}Bi_{0.1}/C$ at potentials higher than 0.60 V vs RHE, the existence of supplementary redox feature in the potential range from 0.10 V to ca. 0.55 V vs RHE with the peak maximum at ca. 0.48 V vs RHE. The redox features between 0.10 to ca. 0.55 V vs RHE occurs in a potential range which is convenient with the potential of 0.48 V vs ESH (standard hydrogen electrode) for the following reaction in aqueous alkaline media[48]:

$$2\ Bi + 6\ OH^- = Bi_2O_3 + 3\ H_2O + 6\ e^- \qquad (5)$$

XPS measurements showed indeed that Bi^0 was present in fresh $Pt_{0.8}Bi_{0.2}/C$ materials. It is then proposed that those redox peaks at low potentials are related to the oxidation/reduction of Bi species less interacting with the Pt surface or having different structures than those leading to the redox features at higher potentials.

To summarize main results from the electrochemical study of Pt_xBi_{1-x}/C materials, different kinds of bismuth atoms coexist in PtBi NPs, those in direct strong interaction with Pt, those in interaction with Bi atoms in strong interaction with Pt, forming small clusters according to molecular dynamics simulations, and those deposited on the carbon surface not in interaction with Pt. Bismuth structures deposited far from platinum are not stable and dissolve upon potential cycles. It can also be stated that the strong interactions between Pt and Bi atoms, as also stipulated from molecular dynamics calculations, leads to electronic effects inhibiting under potential hydrogen deposition reaction and allowing platinum surface oxidation. At last, bismuth atoms in $Pt_{0.9}Bi_{0.1}$/C catalyst are metallic for potentials lower than ca. 0.300 V vs. RHE, are oxidized into Bi^{II} from ca. 0.300 V to ca. 0.800 V vs RHE and into Bi^{III} for higher potentials.

3.4 Electrocatalytic behavior of Pt_xBi_{1-x}/C catalysts.

The electrochemical activities of Pt_xBi_{1-x}/C catalysts in NaOH 0.1 mol L^{-1} N_2-purged electrolyte in the presence of 0.1 mol L^{-1} glycerol, corresponding to the third scans, are compared in Figure 7. For fresh catalysts (Figure 7a), the onset potential, defined as the potential at which the current density of 0.05 mA cm^{-2} is reached, is ca. 0.400 V vs RHE for Pt/C and $Pt_{0.8}Bi_{0.2}$/C, whereas it is decreased down to 0.300 V vs RHE for $Pt_{0.9}Bi_{0.1}$/C. For potential higher than 0.400 V vs RHE, the $Pt_{0.8}Bi_{0.1}$/C catalysts leads to the lower current densities, i.e. to lower catalyst mass activity as all electrodes are loaded with the same mass of metals (100 μg_{metal} cm^{-2}). The important information is that although according the molecular dynamics calculations in part 3.1 and electrochemical study in part 3.3 the Pt surface is expected to be completely covered by bismuth, the $Pt_{0.8}Bi_{0.2}$/C material displays a catalytic activity for glycerol oxidation at high potentials. The $Pt_{0.9}Bi_{0.1}$/C catalyst displays the lowest onset potential and the highest activity (higher current densities from 0.300 V vs RHE than those recorded with Pt/C and $Pt_{0.8}Bi_{0.2}$/C catalysts). Chronoamperometry measurements at

constant voltages (0.55 V and 0.7 V) for the oxidation of 2 M glycerol in 0.5 M NaOH were performed in an electrolysis cell by Cobos-Gonzalez et al.[13] at Pt/C and $Pt_{0.9}Bi_{0.1}$/C (SI 5). $Pt_{0.9}Bi_{0.1}$/C led always to higher initial and stabilized current density over 4 hours of experiments than Pt/C anodes. The higher activity at constant potential indicates lower poisoning of the surface and higher turn-over frequency per Pt sites. Indeed, in this case also molecular dynamics calculations and electrochemical studies showed that the coverage of Pt by Bi was very high. This indicates also that a part of the platinum surface is still available in both cases for the adsorption of glycerol and second that the blocking of hydrogen adsorption is likely related to change in Pt surface electronic density of states implied by the strong interaction with Bi, as predicted by MDs simulation.

The lower activity of $Pt_{0.8}Bi_{0.2}$/C is explained in terms of lower Pt surface available for glycerol electrooxidation. Indeed, the activity towards 0.1 M glycerol electrooxidation of the $Pt_{0.8}Bi_{0.2}$/C catalyst recorded after 1000 potential cycles between 0.05 and 1.00 V in N_2-purged glycerol-free electrolyte tends to that of the $Pt_{0.9}Bi_{0.1}$/C catalyst over the whole studied potential range (Figure 7b), confirming the results in section 3.3 where the CV of $Pt_{0.8}Bi_{0.2}$/C in N_2-purged glycerol free-electrolyte after 1000 potential cycles resembles that of $Pt_{0.9}Bi_{0.1}$/C.

The activity and selectivity of $Pt_{0.9}Bi_{0.1}$/C catalyst for glycerol electrooxidation in alkaline medium is well documented. From *in situ* infrared spectroscopy measurements (SI 6) and HPLC analyses of reaction products after chronoamperometry measurements at different electrolysis cell voltages (SI 5), it has been established that in the low potential range from ca. 0.300 V to ca. 0.600 V vs RHE, glyceraldehyde and dihydroxyacetone are by far the main products formed, whereas for higher potentials, carboxylate species are also formed in significant amounts[13,20] (SI 6.1). The same trends were observed in acidic medium[49]. These works also evidenced that the presence of bismuth avoided the C-C bond breaking, i.e. the formation of C1 and C2 degradation products (SI 6.2).

3.5 Discussion

It is generally recognized that the first step of the electrooxidation at low potentials (lower than 0.4 V vs RHE) of alcohols and polyols, such as ethanol and glycerol, at platinum based-catalysts consists in the dehydrogenation reaction leading to adsorbed aldehyde-like species[50] according to the following general reaction:

in acidic medium: $Pt + R\text{-}CH_2OH \rightarrow Pt\text{-}CHO\text{-}R + 2\ H^+ + 2\ e^-$

in alkaline media: $Pt + R\text{-}CH_2OH + 2\ OH^- \rightarrow Pt\text{-}CHO\text{-}R + 2\ H_2O + 2\ e^-$

But with pure platinum, adsorbed aldehyde is further transformed into adsorbed acetyl-like species that can be oxidized as soon as Pt becomes able to activate water, typically for potentials higher that 0.5 - 0.6 V vs RHE into into carboxylic/carboxylate species and CO_2 (if C-C bond breaking occurs)[51] via the Langmuir-Hinshelwood mechanism. These oxidation processes can be enhanced by modifying platinum with foreign metal atoms, leading to the so-called bifunctional mechanism of electrocatalysis[52], i.e. the third body effect[53]. In the case of $Pt_{0.9}Bi_{0.1}/C$, it is likely that Bi structures participate to this mechanism. It was indeed previously demonstrated by comparing the activity of Pd/C and $Pd_{0.9}Bi_{0.1}/C$ catalysts towards glycerol electrooxidation in alkaline medium[20], that the onset potential was shifted towards lower potentials from ca. 150 mV ($Pd_{0.9}Bi_{0.1}/C$ leading to the same activity as Pt/C), whereas the selectivity towards the formation of carboxylates as main products was the same as for pure Pt. Moreover, the participation of Bi to the third body mechanism also explain the higher current densities recorded on $Pt_{0.9}Bi_{0.1}/C$ than those observed on Pt/C.

At low electrode potentials, the only formation of low oxidized species (mainly glyceraldehyde and a few hydroxyacetone) that don't need the participation of an extra oxygen atom from water activation on Pt surface, indicates clearly that the bifunctional mechanism is not involved. But, assuming the same first steps of glycerol adsorption on $Pt_{0.9}Bi_{0.1}/C$ as on pure Pt/C, the high activity in comparison with the low Pt surface area available for the

adsorption/oxidation reactions also indicates that the turn-over frequency, and further the desorption rate of adsorbed aldehyde species, are enhanced on $Pt_{0.9}Bi_{0.1}$/C material. De Souza et al. [54] also observed that the presence of Bi modified the adsorption energies of adsorbates on Pt surface.

To explain the higher activity for glycerol oxidation and selectivity towards dihydroxyacetone of Bi-modified Pt(111) in acidic medium, Garcia et al. [55] proposed the formation of an enediol intermediate with two carbons adsorbed on two adjacent Pt sites with their alcohol groups interacting with a single Bi adatom. This mechanism is certainly possible in the configuration of Pt surfaces modified by low Bi adatom coverages (θ was between 0.13 and 0.17 in the work of Garcia et al.). However, in the present work, the coverage of Pt seems to be much higher, according to both MDs simulations and electrochemical characterizations, which could prevent the formation of multi-bonded intermediates and favor mainly single-bonded intermediates due to a steric effect, leading mainly to glyceraldehyde at low potentials and glycerate at higher potentials. This observation was also made by De Souza et al.[54] for the glycerol electrooxidation in alkaline medium on Pt electrodes modified by Bi adatoms.

On the other hand, the structure of Bi deposits on Pt surface in the present case differs from that of adatoms in the case of Garcia et al.[55] and De Souza et al.[54]. First, molecular dynamics simulation predicted the formation of Bi dimers and trimers. Second, it was previously clearly shown that the electrochemical behavior of Pd modified by Bi adatoms was very different than that of $Pd_{0.9}Bi_{0.1}$ nanoparticles prepared by the water-in-oil microemulsion method. In the case of Pd nanoparticles modified by Bi adatoms[56], it was previously observed an increase of the current densities for the glycerol electrooxidation from ca. 0.6 V vs RHE, but a small effect on the onset potential. The same behavior, i.e. increase of the activity without significant shift of the onset potential, was observed from ca. 0.4 V vs. RHE by de Souza et al.[54] with Pt electrode modified by Bi adatoms. But, in the case of $Pd_{0.9}Bi_{0.1}$/C nanoparticles prepared by the water-

in-oil microemulsion method[Erreur ! Signet non défini.], the onset potential of glycerol electrooxidation was shifted by ca. 150 mV towards lower values. This discrepancy was explained in terms of different Bi structures deposited on Pd surfaces (adatoms and small amorphous Bi clusters), leading to different interactions between glycerol adsorbates and PdBi surface. This certainly is applicable to Pt surfaces, owing to the very close behavior of both metals (Pd and Pt). Indeed, in the present case, the onset potential of glycerol oxidation is shifted by ca. 150 mV towards lower value on $Pt_{0.9}Bi_{0.1}$/C than on Pt/C.

Adzic[57] proposed that the presence of foreign atom structures at the platinum surface can lead to the dilution the Pt surface atoms, which limits the mean number of adjacent Pt atoms and further the nature of adsorbed species as well as the strength of their adsorption. Moreover, the absence of a typical CO_{ads} infrared absorption band for glycerol oxidation on $Pt_{0.9}Bi_{0.1}$ (SI 6.2) conversely to what is obtained on Pt (multibonded and linearly CO according to the wavenumber value around 1800 cm^{-1} and 2050 cm^{-1}) indicates that the C-C bond breaking, that necessitates several adjacent Pt sites, is avoided in the presence of 10 at% of Bi atoms on Pt nanoparticles.

It is worth to note that the onset potential of glycerol oxidation starts at ca. 0.300 V vs RHE, i.e. at the same potential as that of Bi oxidation onset potential from certainly Bi^0 to Bi^{II}. The early stage of this redox transition seems to be involved in the reaction process not by direct interaction of Bi species with adsorbed species from glycerol but by changing the electronic surface state of platinum, leading to lower the bonding strength between Pt sites and adsorbed aldehyde/ketone species, and at last by favoring their desorption. This reaction allows liberating Pt sites for further adsorption of glycerol and iterations of the different reaction steps. This mechanism involving both a geometric effect (dilution of adjacent Pt atoms) and a strong electronic effect between Pt and Bi, as predicted from MDs simulations, explains both the high

activity of $Pt_{0.9}Bi_{0.1}$/C catalyst at low potentials and its high selectivity towards low oxidized species.

4. Conclusion

Pt/C, $Pt_{0.9}Bi_{0.1}$/C and $Pt_{0.8}Bi_{0.2}$/C materials were synthesized at room temperature using a microemulsion method and their nature and structure were characterized by different physicochemical and electrochemical methods. In order to gain insight on the final structure of materials, results from physicochemical characterization were compared to predictions from molecular dynamics simulations. From physicochemical characterizations, and particularly XRD measurements before and after potential cycling, Pt_xBi_{1-x} materials appeared to consist in Pt nanoparticles of ca. 4 - 5 nm diameter decorated by bismuth structures. From MDs, the final structures of Pt_xBi_{1-x} nanoparticles consisted in a crystalline Pt core surrounded by Bi atoms, forming dimers and trimers depending on the Bi to Pt ratio. The growth dynamics showed a systematic Bi segregation towards the Pt core surface. This is consistent with the shape of the interaction potential vs distance curves showing a minimum at shorter distance for Pt-Pt interaction than for Pt-Bi interaction, which should favor the formation of a Pt core. Stronger Pt-Bi interaction (deeper well) at larger distance than that for Pt-Pt is responsible for Bi location on the outer Pt nanoparticle surface. Both physicochemical and simulation methods lead to consistent results, confirming the Pt core Bi shell structure of the nanoparticles.

$Pt_{0.9}Bi_{0.1}$/C has demonstrated the highest activity towards glycerol electrooxidation with an oxidation onset potential shifted by ca. 0.250 V towards lower values compared with that obtained with Pt/C. In addition, to the high activity at low potentials, $Pt_{0.9}Bi_{0.1}$/C is also very selective towards glyceraldehyde/hydroxyacetone for potentials lower than 0.6 V vs RHE. Such selectivity cannot be explained by the ability of bismuth to adsorb OH species, because the bifunctional mechanism is not effective in the considered potential range. It is then explained in terms of lowering of the aldehyde/ketone-like absorbed species at platinum sites

owing to the strong interaction between bismuth and platinum. MDs also predicted strong electronic interaction between Pt and Bi, leaning on the deep interaction potential well for Pt-Bi. This strong electronic effect together with the one-carbon adsorption mode due to dilution of Pt sites by bismuth structures (ensemble effect) favor the formation of glyceraldehyde/dihydroxyacetone and their desorption. In addition, the enhancement of the desorption rate is driven by the early stage of the Bi^0/Bi^{II} transition, which will certainly affect the electronic state of platinum surface. Now, the understanding of the role of the Bi redox transition in the electronic change of Pt surface and further in activity/selectivity enhancement brought by Bi is, in our opinion, the next important step to be able to design the best catalysts for biomass electro-reforming.

Although MDs simulation were useful to determine the structure of Pt_xBi_{1-x} nanomaterials, this simulation method can't represent totally the reality, because it is physically impossible to take into account all parameters (in terms of calculation time and data processing). It is then a simplification allowing to propose general trends, and in the present case those relative to the structures and possible electronic interactions between atoms during the nanoparticle formation, only based on known and relevant interaction potentials between atoms (Pt-Pt, Bi-Bi and Pt-Bi). Therefore, some differences between simulated and real materials, such as the final size, arise, which could affect electronic and geometric effects and hence the catalyst behavior. This is the reason why MD simulations in the present article have not the ambition to simulate the electrochemical and electrocatalytic behaviors of Pt_xBi_{1-x} nanostructures, but only that to confirm the initial structures of catalysts (which is maintained over the long-term electrochemical experiments).

Acknowledgements

This work was partly funded by the ANR project ECO-PLAN under grant ANR-16-CE29-0007. The authors thank the European communities (FEDER, Econat Project) and the "Région

Nouvelle Aquitaine" for financial support. PB gratefully acknowledges G. Raos (Ref. [29]) for providing us with Bi-Bi EAM potential data file. CC and SB acknowledge Dr. Mario Simoes, Dr. Anna Zalineeva and Dr. Jesus Cobos-Gonzalez for previous experimental contributions.

References

1. A. Tathod, T. Kane, E.S. Sanil, P. L. Dhepe. Solid base supported metal catalysts for the oxidation and hydrogenation of sugars. J. Mol. Catal. A: Chemical 388–389 (2014) 90–99
2. E. Bahcegul, H. E. Toraman, N. Ozkan, U. Bakir. Evaluation of alkaline pretreatment temperature on a multi-product basis for the co-production of glucose and hemicellulose-based films from lignocellulosic biomass. Bioresour. Techn. 103 (2012) 440–445.
3. M. A. Dasari, P. P. Kiatsimkul, W. R. Sutterlin, G. J. Suppes. Low-pressure hydrogenolysis of glycerol to propylene glycol. Appl. Catal. A: General. 281 (2005) 225– 231.
4. R. Ciriminna, C. Della Pina, M. Rossi, Mario Pagliaro. Understanding the glycerol market. Eur. J. Lipid Sci. Technol. 116 (2014) 1432–1439
5. P. Gallezot, Selective oxidation with air on metal catalysts, Catal. Today 37 (1997) 405 – 418.
6. M. J. Climent, A. Corma, S. Iborra. Converting carbohydrates to bulk chemicals and fine chemicals over heterogeneous catalysts. Green Chem. 13 (2011) 520–540.
7. A. Behr, J. Eilting, K. Irawadi, J. Leschinski, F. Lindner. Improved utilisation of renewable resources: New important derivatives of glycerol. Green Chem. 10 (2008) 13–30.
8. S. Hermans, A. Deffernez, M. Devillers. Au–Pd/C catalysts for glyoxal and glucose selective oxidations. ACS Sustainable Chem. Eng. 4 (2016) 2432−2438.
9. S. Carrettin, P. Mc Morn, P. Johnston, K. Griffin, C. J. Kielyc, G. A. Attard, G. J. Hutchings. Oxidation of glycerol using supported gold catalysts. Top. Catal. 27 (2004) 131–136.

10. V. Bambagioni, M. Bevilacqua, C. Bianchini, J. Filippi, A. Lavacchi, A. Marchionni, F. Vizza, P. K. Shen. Selfsustainable production of hydrogen, chemicals, and energy from renewable alcohols by electrocatalysis. ChemSusChem 3 (2010) 851–855.
11. M. Simões, S. Baranton, C. Coutanceau, Electrochemical Valorisation of Glycerol, ChemSusChem 5 (2012) 2106 – 2124.
12. Y. X. Chen, A. Lavacchi, H. A. Miller, M. Bevilacqua, J. Filippi, M. Innocenti, A. Marchionni,W. Oberhauser, L. Wang, F. Vizza, Nanotechnology makes biomass electrolysis more energy efficient than water electrolysis, Nature Comm. 5 (2014) 4036 1-6.
13. J. Cobos-Gonzalez, S. Baranton, C. Coutanceau. Development of Bi-Modified PtPd Nanocatalysts for the Electrochemical Reforming of Polyols into Hydrogen and Value-Added Chemicals. ChemElectroChem 3 (2016) 1694–1704.
14. Z. Zhang, L. Xin, W. Li. Electrocatalytic oxidation of glycerol on Pt/C in anion-exchange membrane fuel cell: Cogeneration of electricity and valuable chemicals. Appl. Catal. B: Environmental 119–120 (2012) 40–48.
15. T. Rafaïdeen, S. Baranton, C. Coutanceau. Highly efficient and selective electrooxidation of glucose and xylose in alkaline medium at carbon supported alloyed PdAu nanocatalysts. Appl. Catal. B: Environmental 243 (2019) 641–656.
16. T. Mallat, A. Baiker, Oxidation of alcohols with molecular oxygen on platinum metal catalysts in aqueous solutions, Catal. Today 19 (1994) 247 – 284.
17. A. Zalineeva, M. Padilla, U. Martinez, A. Serov, K. Artyushkova, S. Baranton, C. Coutanceau, P. B. Atanassov. Self-Supported Pd_xBi Catalysts for the Electrooxidation of Glycerol in Alkaline Media. J. Am. Chem. Soc. 136 (2014) 3937–3945.

18. E. Casado-Rivera, D. J. Volpe, L. Alden, C. Lind, C. Downie, T. Vázquez-Alvarez, A. C. D. Angelo, F. J. DiSalvo, H. D. Abrunã. Electrocatalytic Activity of Ordered Intermetallic Phases for Fuel Cell Applications. J. Am. Chem. Soc. 126 (2004) 4043 – 4049.

19. C. Roychowdhury, F. Matsumoto, P. F. Mutolo, H. D. Abrunã, F. J. DiSalvo, Synthesis, Characterization, and Electrocatalytic Activity of PtBi Nanoparticles Prepared by the Polyol Process, Chem. Mater. 17 (2005) 5871 – 5876.

20. M. Simões, S. Baranton, C. Coutanceau, Enhancement of catalytic properties for glycerol electrooxidation on Pt and Pd nanoparticles induced by Bi surface modification, Applied Catalysis B: Environmental 110 (2011) 40 – 49.

21. M. Wojdyr. Fityk: a general-purpose peak fitting program. J. Appl. Crystallogr. 43 (2010) 1126−1128.

22. P. Brault, E. Neyts, Molecular dynamics simulations of supported metal nanocatalyst formation by plasma sputtering, Catal. Today 256 (2015) 3 – 12

23. P. Brault, C. Coutanceau, P. C. Jennings, T. Vegge, J. Berndt, A. Caillard, S. Baranton, S. Lankiang, Molecular dynamics simulations of ternary $Pt_xPd_yAu_z$ fuel cell nanocatalyst growth. Int. J. Hydrogen Energy 41 (2016) 22589 – 22597

24. H. Okamoto, The Bi-Pt (Bismuth-Platinum) System. J. Phase Equilibria 12 (1991) 207 – 210.

25. A. Caillard, S. Cuynet, T. Lecas, P. Andreazza, M. Mikikian, A. –L. Thomann, P. Brault, PdPt catalyst synthesized using a gas aggregation source and magnetron sputtering for fuel cell electrodes. J. Phys D: Applied Physics 48 (2015) 475302.

26. E. Quesnel, E. Pauliac-Vaujour, V. Muffato. Modeling metallic nanoparticle synthesis in a magnetron-based nanocluster source by gas condensation of a sputtered vapor. J. Appl. Phys. 107 (2010) 054309.

27. X. Zhou, R. Johnson, H. Wadley. Misfit-energy-increasing dislocations in vapor-deposited CoFe/NiFe multilayers. Phys. Rev. B 69 (2004) 144113.

28. D. K. Belashchenko. Computer Simulation of the Properties of Liquid Metals: Gallium, Lead, and Bismuth. Russ. J. Phys. Chem. A 86 (2012) 779-790.

29. Y. Gao, G. Raos, C. Cavallotti, M. Takahashi. Molecular Dynamics Simulation on Physical Properties of Liquid Lead, Bismuth and Lead-bismuth Eutectic (LBE). Procedia Engineering 157 (2016) 214 – 221.

30. S. M. Foiles, M. I. Baskes, M. S. Daw. Embedded-atom-method functions for the fcc metals Cu, Ag, Au, Ni, Pd, Pt, and their alloys. Phys. Rev. B 33 (1986) 7983; Erratum: Phys. Rev. B 37 (1988) 10378.

31. M. S. Daw, S. M. Foiles, M. I. Baskes. The embedded-atom method: a review of theory and applications. Mat. Sci. Reports 9 (1993) 251–310.

32. R. A. Johnson. Alloys models with the embedded-atom method. Phys. Rev. B 39 (1989) 12554.

33. J. Solla-Gullón, P. Rodríguez, E. Herrero, A. Aldaz, J. M. Feliu, Surface characterization of platinum electrodes. Phys. Chem. Chem. Phys. 10 (2008) 1359–1373.

34. H. Zhu, X. Li, F. Han, Z. Dong, G. Yuan, G. Ma, A. Westwood, K. He. The effect of pitch-based carbon fiber microstructure and composition on the formation and growth of SiC whiskers via reaction of such fibers with silicon sources. Carbon 99 (2016) 174−185.

35. H. Yi, H. Wang, Y. Jing, T. Peng, Y. Wang, J. Guo, Q. He, Z. Guo, X. Wang,.Advanced asymmetric supercapacitors based on CNT@$Ni(OH)_2$ core-shell composites and 3D graphene networks. J. Mater. Chem. A 3 (2015) 19545−19555

36. J. Hou, C. Yang, Z. Wang, W. Zhou, S. Jiao, H. Zhu. In situ synthesis of α–β phase heterojunction on Bi_2O_3 nanowires with exceptional visible-light photocatalytic performance. Applied Catalysis B: Environmental 142–143 (2013) 504–511.

37. B. E. Warren, X-Ray Diffraction; Dover Publications, Inc., New York (1990) pp. 251-254.

38. J. C. Slater. Atomic Radii in Crystals. J. Chem. Phys. 10 (1964) 3199–3204.

39. P. J. Cumpson, M. P. Seah. Elastic Scattering Corrections in AES and XPS. II. Estimating Attenuation Lengths and Conditions Required for their Valid Use in Overlayer/Substrate Experiments. Suf. Interface Anal. 25 (1997) 430–446.

40. W. Zuo, W. Zhu, D. Zhao, Y. Sun, Y. Li, J. Liu, X. W. Lou. Bismuth oxide: a versatile high-capacity electrode material for rechargeable aqueous metal-ion batteries. Energy Environ. Sci. 9 (2016) 2881 – 2891.

41. H. Kimura, K. Tsuto, T. Wakisaka, Y. Kazumi, Y. Inaya. Selective oxidation of glycerol on a platinum-bismuth catalyst. Appl. Catal. A 96 (1993) 217 – 228.

42. J. Clavilier, J. -M. Feliu, A. Aldaz, An irreversible structure sensitive adsorption step in Bismuth uderpotential deposition at platinum electrodes. J. Electroanal. Chem., 243 (1988) 419 – 433.

43. S. Blais, G. Jerkiewicz, E. Herrero, J. M. Feliu. New insight into the electro-oxidation of the irreversibly chemisorbed bismuth on Pt(111) through temperature-dependent research. J. Electroanal. Chem. 519 (2002) 111–122.

44. M. M. Tusi, N. S. O. Polanco, S. G. Da Silva, E. V. Spnacé, A. O. Nato. The high activity of PtBi/C catalyst for ethanol electro-oxidation in alkaline media. Electrochem. Comm. 13 (2011) 143 – 146.

45. F. Kadirgan, B. Beden, C. Lamy. J. Electroanal. Chem. Electrocatalytic oxidation of ethylene-glycol. Part II. Behaviour of platinum ad-atom electrodes in alkaline medium. 143 (1983) 135–152.

46. A. Zadick, L. Dubau, N. Sergent, G. Berthomé, M. Chatenet. Huge Instability of Pt/C Catalysts in Alkaline Medium. ACS Catal. 5 (2015) 4819−4824.

47. S. Cherevko, A. R. Zeradjanin, G. P. Keeley, K. J. J. Mayrhofer. A Comparative Study on Gold and Platinum Dissolution in Acidic and Alkaline Media. J. Electroch. Soc. 161 (2014) H822-H830.

48. J. Van Muylder, M. Pourbaix, Atlas d'équilibres électrochimiques à 25 ◦C, Gauthier-Villars & Cie, Paris, 1963.

49. Y. Kwon, Y. Birdja, I. Spanos, P. Rodriguez, M. T. M. Koper. Highly Selective Electro-Oxidation of Glycerol to Dihydroxyacetone on Platinum in the Presence of Bismuth. ACS Catal. 2 (2012) 759−764.

50. F. Vigier, C. Coutanceau, F. Hahn, E.M. Belgsir, C. Lamy. On the mechanism of ethanol electro-oxidation on Pt and PtSn catalysts: electrochemical and in situ IR reflectance spectroscopy studies. J. Electroanal. Chem. 563 (2004) 81 – 89.

51. F. Vigier, S. Rousseau, C. Coutanceau, J.- M. Léger, C. Lamy. Electrocatalysis for the direct alcohol fuel cell. Top. Catal. 40 (2006) 111 – 121.

52. M. Watanabe, S. Motoo. Electrocatalysis by ad-atoms. 2. Enhancement of oxidation of methanol on platinum by ruthenium ad-atoms. J. Electroanal. Chem. 60 (1975) 267−273.

53. T. J. Schmidt, R. J. Behm, B. N. Grgur, N. M. Markovic, P. N. Ross Jr. Formic Acid Oxidation on Pure and Bi-Modified Pt(111): Temperature Effects. Langmuir 16 (2000) 8159−8166.

54. M. B. C. de Souza, R. A. Vicente, V. Y. Yukuhiro, C. T. G. V. M. T. Pires, W. Cheuquepan, J. L. Bott-Neto, J. Solla-Gullon, P. S. Fernandez. Bi-modified Pt Electrodes toward Glycerol Electrooxidation in Alkaline Solution: Effects on Activity and Selectivity. ACS Catal. 9 (2019) 5104−5110.

55. A. C. Garcia, Y. Y. Birdja, G. Tremiliosi-Filho, M. T .M. Koper, Glycerol electro-oxidation on bismuth-modified platinum single crystals. J. Catalysis 346 (2017) 117–124.

56. C. Coutanceau, A. Zalineeva, S. Baranton, M. Simoes. Modification of palladium surfaces by bismuth adatoms or clusters: Effect on electrochemical activity and selectivity towards polyol electrooxidation. Int. J Hyd. energy 39 (2014) 15877–15886.

57. R. R. Adzic, (1984). “Electrocatalysis on surfaces modified by foreign metal adatoms,” in Advances in Electrochemistry and Electrochemical Engineering, eds. H. Gerisher, C. W. Tobias (New York: Wiley- Interscience), 159−260.

Table 1. Physicochemical characterization data obtained for Pt/C, $Pt_{0.9}Bi_{0.1}$/C and $Pt_{0.8}Bi_{0.2}$/C.

	Pt/C	$Pt_{0.9}Bi_{0.1}$/C		$Pt_{0.8}Bi_{0.2}$/C	
Metal loading TGA (wt%)	40.5	43.5		37.5	
Composition ICP-OES (at%)	100	Pt	Bi	Pt	Bi
		92	8	84	16
Composition AAS (at%)	100	Pt	Bi	Pt	Bi
		88.2	11.8	78.2	21.8
Particle size (nm)	5.2	4.7		4.7	
Crystallite size (nm)	3.5	4.3		3.1	
Cell parameter (nm)	0.3916	0.3919		0.3926	
Composition XPS (at%) Fresh catalysts		Pt^0: 79	Bi_{total}: 21	Pt^0: 72	Bi_{total}: 28
			$Bi(OH)_2$: 72 % $Bi(OH)_3$: 22% Bi_2O_4: 6%		Bi^0 9 % $Bi(OH)_2$: 34% $Bi(OH)_3$: 51% Bi_2O : 6%
Composition XPS (at%) Catalysts after 10 potential cycles		Pt^0: 79	Bi_{total}: 21	Pt^0: 71	Bi_{total}: 29
			$Bi(OH)_2$: 87 % $Bi(OH)_3$: 8% Bi_2O_4: 5%		$Bi(OH)_2$: 69% $Bi(OH)_3$: 20% Bi_2O_4: 11%

Figure caption

Figure 1. Plots of the pair part of the interaction potentials as a function of the interatomic distance (r) used in the MD simulations. blue line: $V_{PtPt}(r)$; red line: $V_{BiBi}(r)$; grey line: $V_{PtBi}(r)$.

Figure 2. Snapshot of the final clusters at 10 ns. Argon atom (4000) are not represented for clarity. $(n_{Pt} + n_{Bi}) = 500$. (a) Pt alone (b) $Pt_{0.9}Bi_{0.1}$ (c) $Pt_{0.8}Bi_{0.2}$.

Figure 3. (a,b,c) TEM images and (d,e,f) corresponding histograms of particle size distribution from TEM observations on (a,d) Pt/C, (b,e) $Pt_{0.9}Bi_{0.1}$/C and (c,f) $Pt_{0.8}Au_{0.2}$/C.

Figure 4. XRD diffraction patterns of Pt/C (black line), $Pt_{0.9}Bi_{0.1}$/C (red line) and $Pt_{0.}t_8Bi_{0.2}$/C catalysts (blue line).

Figure 5. XPS spectra for Pt 4f and Bi 4f orbitals (a,b) on fresh $Pt_{0.9}Bi_{0.1}$/C, (c,d) on fresh $Pt_{0.8}Bi_{0.2}$/C catalysts, (e,f) on cycled $Pt_{0.9}Bi_{0.1}$/C and (g,h) on cycled $Pt_{0.8}Bi_{0.2}$/C (10 voltammetric cycles between 0.05 and 1.00 V vs RHE at 20°C in 0.1 M NaOH electrolyte).

Figure 6. (a) Tenth stable cyclic voltammograms of Pt/C (black line), $Pt_{0.9}Bi_{0.1}$/C (red line) and $Pt_{0.8}Bi_{0.2}$/C (blue line) materials and (b) cyclic voltammograms recorded after 1000 potential cycles between 0.05 and 1.20 V vs RHE at 50 mV s^{-1} on $Pt_{0.9}Bi_{0.1}$/C (red line) and $Pt_{0.8}Bi_{0.2}$/C (blue line) materials (v = 5 mV s^{-1}, N_2-saturated 0.1 M NaOH electrolyte, T = 20 °C).

Figure 7. (a) Polarization curves of 0.1 M glycerol oxidation recorded (a) after 10 potential cycles between 0.05 and 1.00 V in N_2-purged glycerol-free electrolyte at Pt/C (black line), $Pt_{0.9}Bi_{0.1}$/C (red line) and $Pt_{0.8}Bi_{0.2}$/C (blue line) materials (v = 5 mV s^{-1}, N_2-saturated 0.1 M NaOH electrolyte, T = 20 °C); (b) after 1000 cycles between 0.05 and 1.00 V in N_2-purged glycerol-free electrolyte at $Pt_{0.9}Bi_{0.1}$/C (red line) and $Pt_{0.8}Bi_{0.2}$/C (blue line) catalysts (v = 5 mV s^{-1}, N_2-saturated 0.1 M NaOH electrolyte, T = 20 °C).

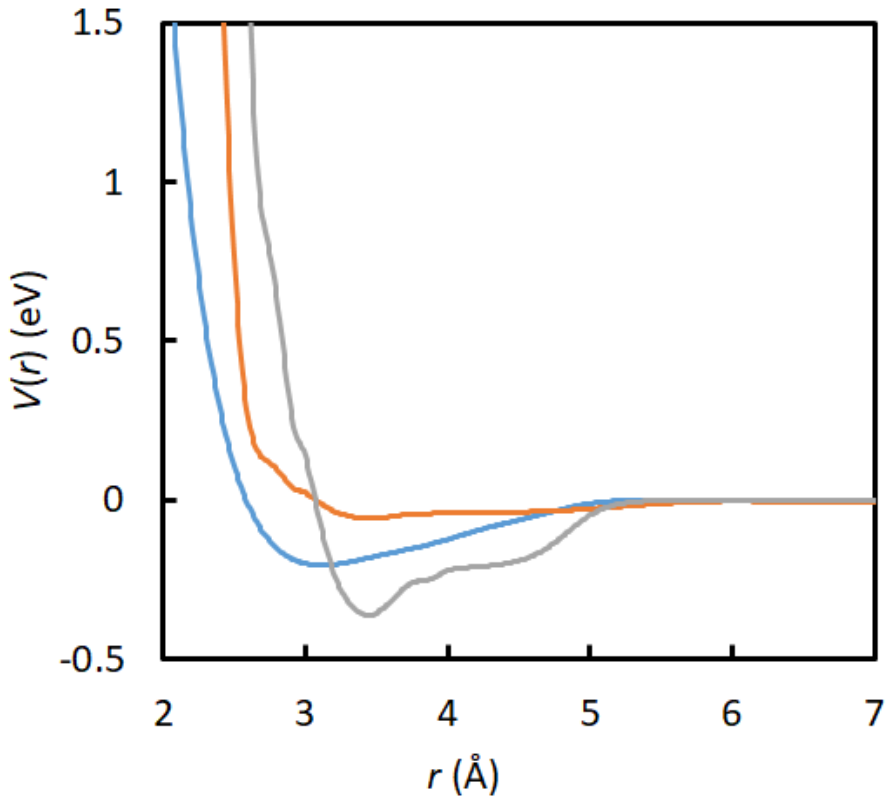

Figure 1

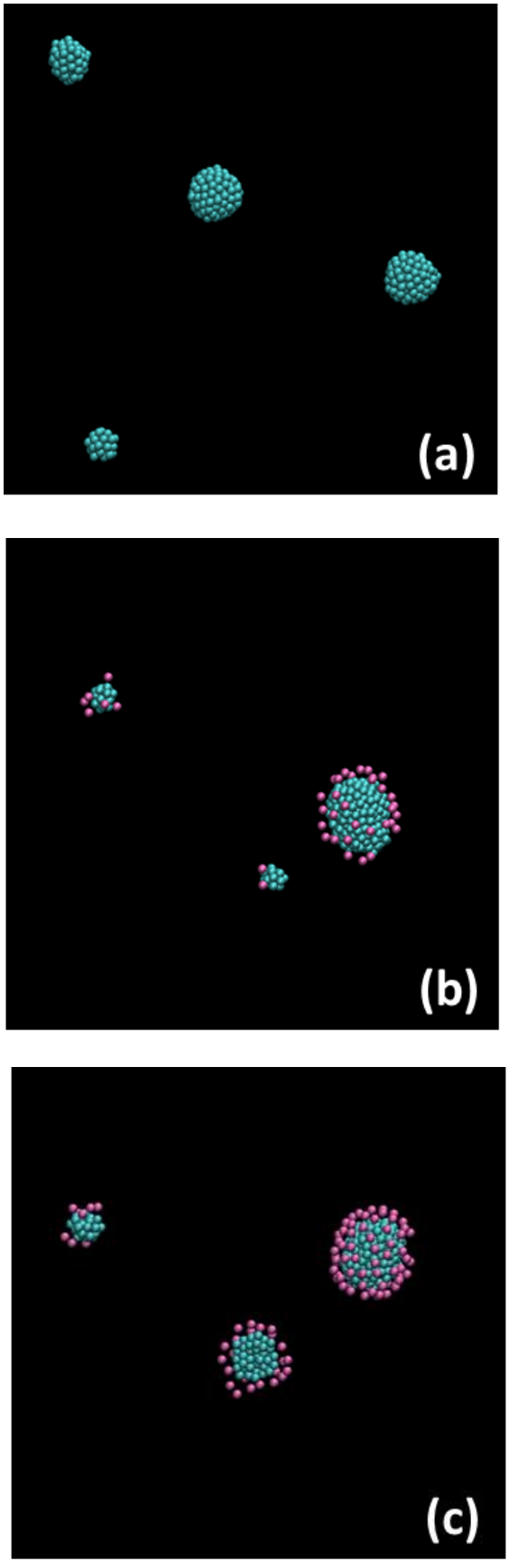

Figure 2

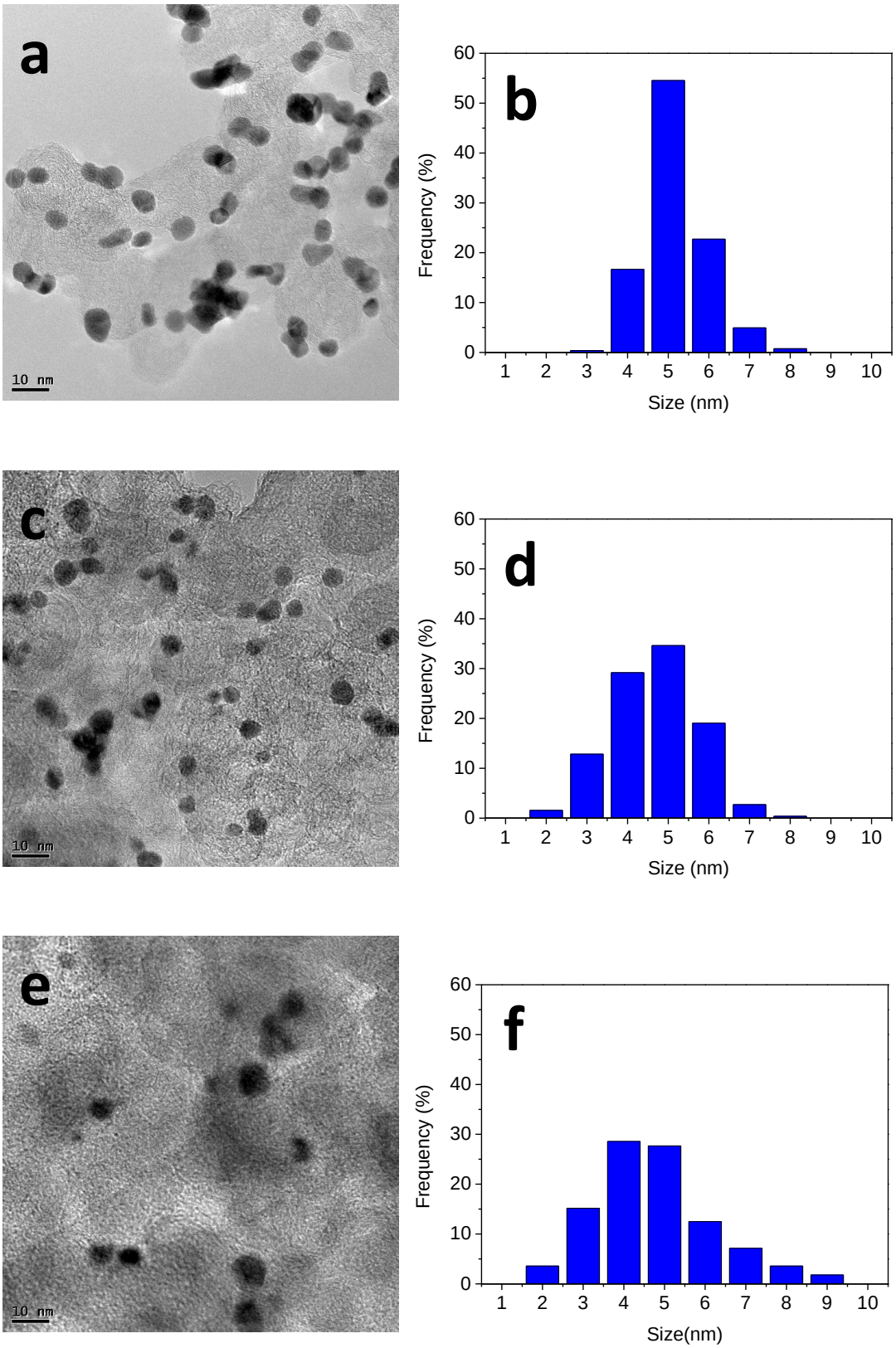
a
10 nm
b
Frequency (%)
Size (nm)
c
10 nm
d
Frequency (%)
Size (nm)
e
10 nm
f
Frequency (%)
Size(nm)

Figure 3

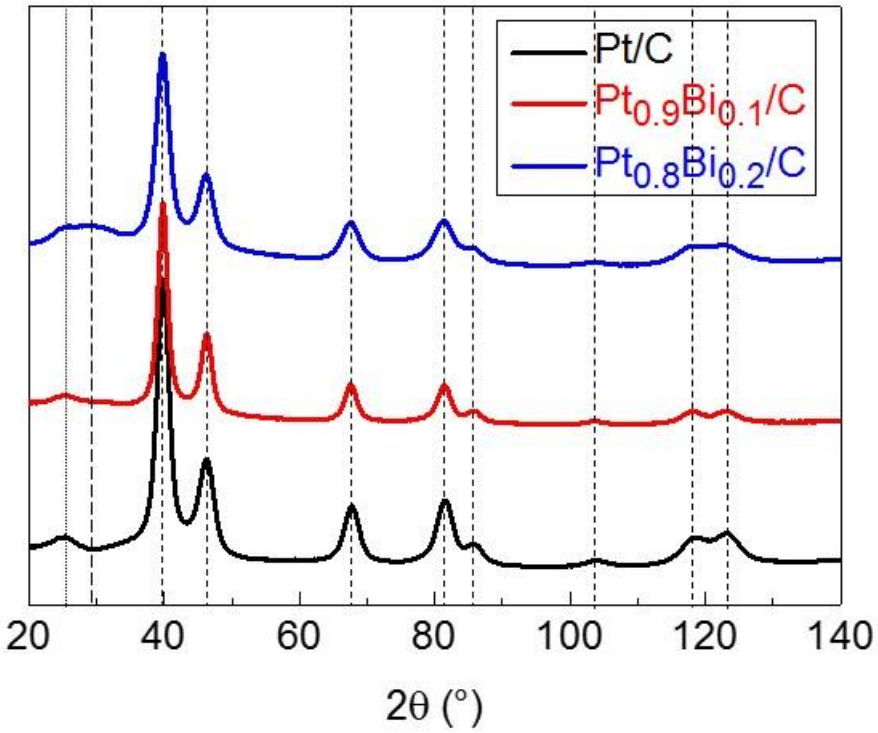

Figure 4

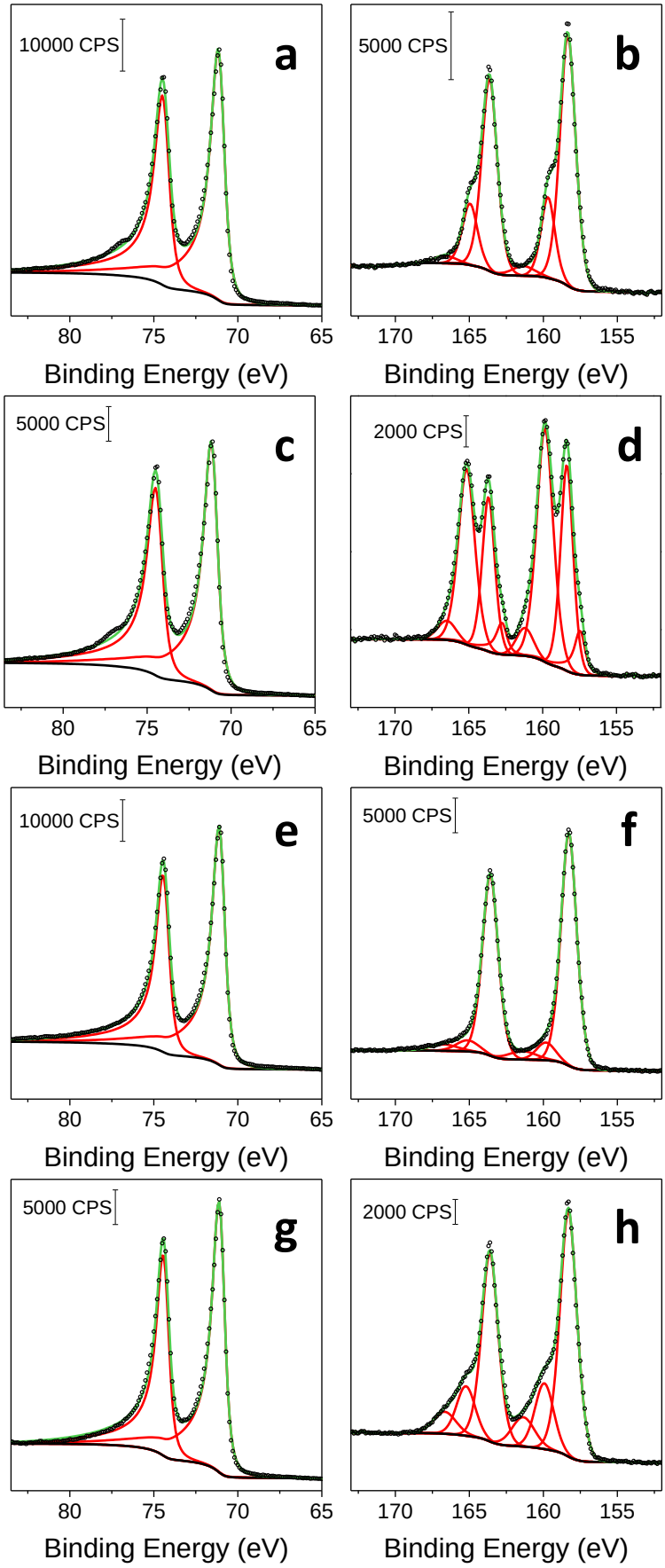
10000 CPS
a
80
75
70
65
Binding Energy (eV)
5000 CPS
b
170
165
160
155
Binding Energy (eV)
5000 CPS
c
80
75
70
65
Binding Energy (eV)
2000 CPS
d
170
165
160
155
Binding Energy (eV)
10000 CPS
e
80
75
70
65
Binding Energy (eV)
5000 CPS
f
170
165
160
155
Binding Energy (eV)
5000 CPS
g
80
75
70
65
Binding Energy (eV)
2000 CPS
h
170
165
160
155
Binding Energy (eV)

Figure 5

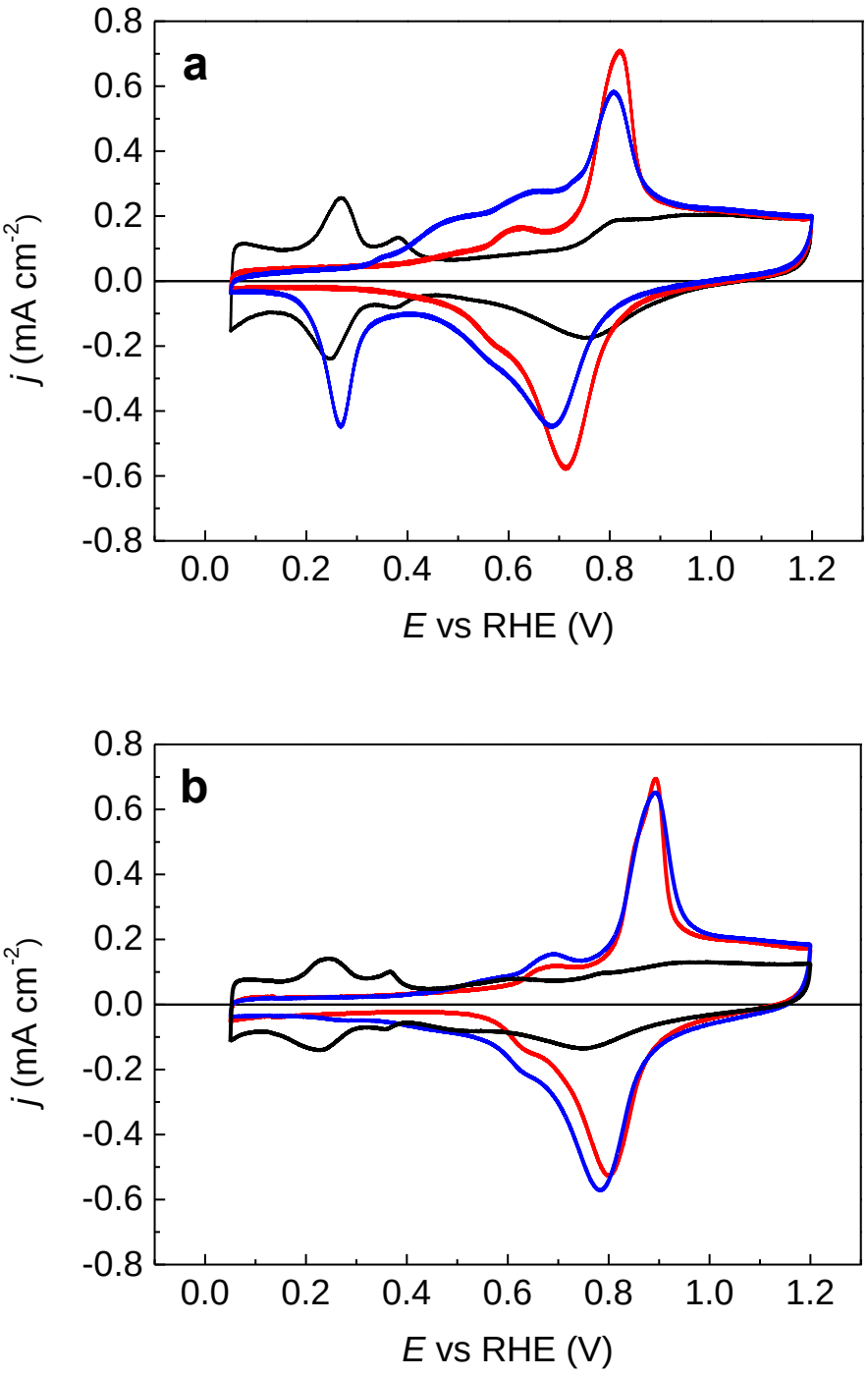

Figure 6

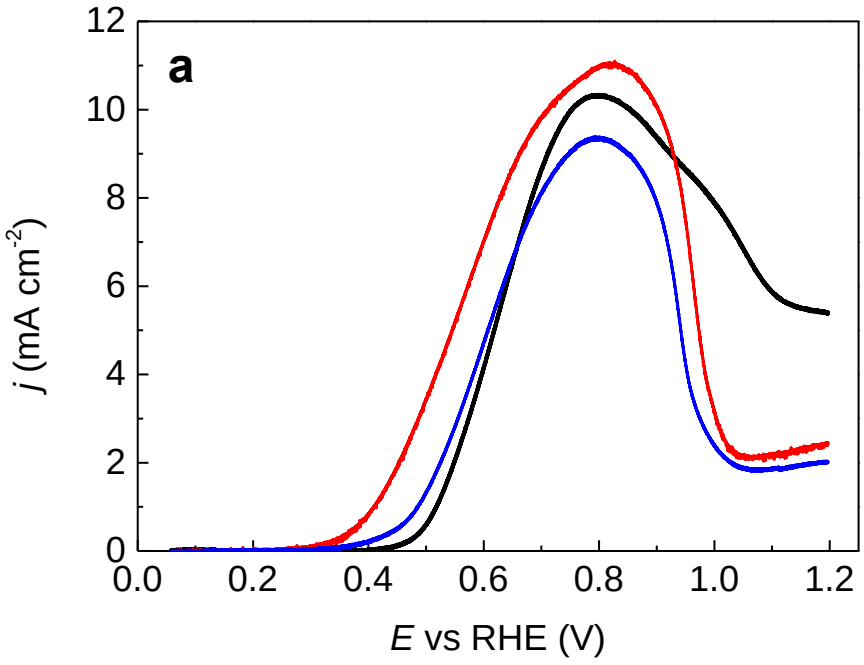
a
12
10
8
6
4
2
0
0.0
0.2
0.4
0.6
0.8
1.0
1.2
j (mA cm-2)
E vs RHE (V)

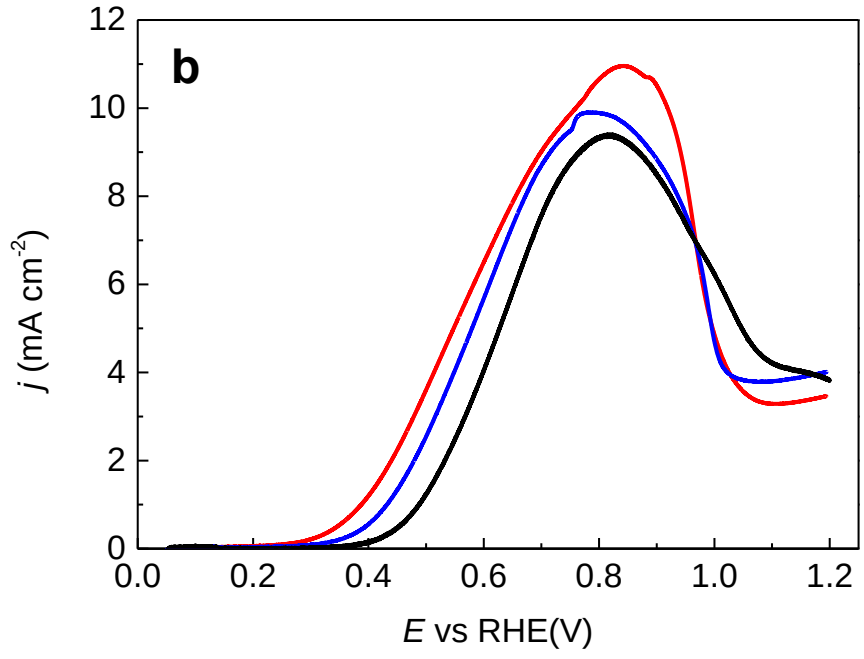
b
12
10
8
6
4
2
0
0.0
0.2
0.4
0.6
0.8
1.0
1.2
j (mA cm-2)
E vs RHE(V)

Figure 7